Materials Today Bio 20 (2023) 100688

Contents lists available at ScienceDirect

Materials Today Bio

journal homepage: www.journals.elsevier.com/materials-today-bio

Novel one-pot strategy for fabrication of a pH-Responsive bone-targeted drug self-frame delivery system for treatment of osteoporosis☆

Xinmin Yang [a,c,1], Xiaowei Yang [a,c,1], Peng Luo [a,c], Yanlong Zhong [a,c], Bin Zhang [a], Weifeng Zhu [b], Meiying Liu [b,**], Xiaoyong Zhang [c,***], Qi Lai [a,*], Yen Wei [d]

[a] Department of Orthopedics, First Affiliated Hospital of Nanchang University, No. 17 Yong Wai Zheng Street, Nanchang, Jiangxi, 330006, China
[b] Key Laboratory of Modern Chinese Medicine Preparation of Ministry of Education, Jiangxi University of Traditional Chinese Medicine, Nanchang, Jiangxi, 330004, China
[c] Department of Chemistry, Nanchang University, 999 Xuefu Avenue, Nanchang, 330031, China
[d] Department of Chemistry and the Tsinghua Center for Frontier Polymer Research, Tsinghua University, Beijing, 100084, PR China

ARTICLE INFO

Keywords:
Bone targeting
Self-framing drug delivery system
pH responsiveness
Natural compounds-based drug delivery systems

ABSTRACT

Osteoporosis (OP) is a systemic metabolic orthopedic disorder prevalent in elderly people, that is characterized by a decrease in bone mass. Although many therapeutics have been adopted for OP treatment, many of them are still not well satisfied clinical requirements and therefore development of novel therapeutics is of great significance. In this work, a novel bone-targeting drug self-frame delivery system (DSFDS) with high drug loading efficiency and pH responsive drug release was fabricated by condensation of curcumin (Cur), amino group terminated polyethylene glycol (NH_2-PEG), and alendronate (ALN) using hexachlorocyclotriphosphonitrile (HCCP) as the linker. The final product named as HCCP-Cur-PEG-ALN (HCPA NPs) displayed excellent water dispersity with small size (181.9 ± 25.9 nm). Furthermore, the drug loading capacity of Cur can reach 25.8%, and Cur can be released from HCPA NPs under acidic environment. Owing to the introduction of ALN, HCPA NPs exhibited strong binding to HAp *in vitro* and excellent bone-targeting effect *in vivo*. Results from cellular and biochemical analyses revealed that HCPA NPs could effectively inhibit the formation and differentiation function of osteoclasts. More importantly, we also demonstrated that HCPA NPs could effectively reduce bone loss in OVX mice with low toxicity to major organs. The above results clearly demonstrated that HCPA NPs are promising for OP treatment. Given the simplicity and well designability of fabrication strategy, explicit therapy efficacy and low toxicity of HCPA NPs, we believe that this work should be of great interest for fabrication of various DSFDS to deal with many diseases.

1. Introduction

Osteoporosis (OP), a systemic metabolic orthopedic disorder prevalent in the elderly people, is characterized by a decrease in bone mass, a progressive decrease in bone mineral density, and the degradation of the microarchitecture of bone tissue, thus leading to a significant increase in the risk of fracture [1–4]. Previous studies showed that maintaining normal bone density is highly depended on a metabolic balance between bone formation and bone resorption [5,6]. When osteoclast-mediated bone resorption is abnormally active, it may cause pathological bone loss and thereby accelerating the disease process [7,8]. Currently, clinically used anti-bone resorption drugs such as bisphosphonates, disulfiramab, and selective estrogen receptor modulators have limited therapeutic effects and will also result in side effects on the kidney, liver, and gastrointestinal tract [9–12]. Due to their low toxicity, easy accessibility, and wide range of pharmacological effects, natural compounds (NC) have recently attracted great research attention of scientists for OP treatment [13,14]. Among them, the polyphenolic compound curcumin (Cur) exerts antiosteoporosis therapeutic effects by modulating a variety of target molecules involved in bone remodeling regulation, such as nuclear factor kappa Beta (NF-κB), activating protein-1, tumor necrosis factor α (TNF-α), interleukin-1 (IL1) and interleukin-6 (IL6) [15–17].

☆ Qi Lai is the corresponding author, Meiying Liu, Xiaoyong Zhang are co-corresponding authors.
* Corresponding author.
** Corresponding author.
*** Corresponding author.
E-mail addresses: lmy5305@iccas.ac.cn (M. Liu), zhangxiaoyong@ncu.edu.cn (X. Zhang), 15879177108@163.com (Q. Lai).
[1] The two authors are contributed equally to this work.

https://doi.org/10.1016/j.mtbio.2023.100688
Received 28 March 2023; Received in revised form 27 May 2023; Accepted 2 June 2023
Available online 3 June 2023

However, the clinical application of Cur for OP treatment still has some disadvantages, such as poor absorption in the gastrointestinal tract, short plasma half-life, and low bioavailability [18–20].

Therefore, the development of novel drug delivery systems to address the above issues has become the research focus from different disciplines over the past few decades. It has been demonstrated that the application of nano drug delivery systems could not only improve the pharmacokinetic properties and biodistribution behavior of drugs, but also endow drugs with novel features and functions [21]. Therefore, nano drug delivery carriers are expected to improve the therapeutic efficacy, attenuate the toxicity of drugs and result in synergistic therapy effects. Different organic nanocarriers such as lipid nanoparticles, polymeric nanoparticles, and inorganic nanocarriers such as gold nanoparticles (AuNPs) and silica nanoparticles (SiNPs) have been previously developed for this aim [22–32]. However, most of the above mentioned nanocarriers themselves do not possess therapeutic effects on OP, and degradation, metabolism, and excretion of these carriers may cause potential toxicity [33–35]. Furthermore, the preparation process of these drug delivery systems is relatively cumbersome, and the drug loading capacity is often unsatisfactory [36,37]. Therefore, development of more efficient, biocompatible, and multifunctional nanocarriers for OP treatment is highly desirable. Recently, drug self-frame delivery systems (DSFDS) have received increasing attention because they are constructed with the participation of free drug molecules without the need for additional nanocarriers [38]. DSFDS form particles with nanoscales by self-assembly between multiple active drugs, which achieve intracellular delivery independently without relying on nanocarriers [39–43]. In Hou's study, the authors successfully prepared a DSFDS for cancer treatment with a drug loading capacity of up to 87.1% by polymerization of HCCP and doxorubicin (DOX) [44].

In this work, we proposed a novel and simple strategy by using hexachlorocyclotriphosphonitrile (HCCP) as inorganic backbone to covalently link Cur by condensation reaction to fabricate DSFDS with higher stability, high drug loading capacity, and pH responsive drug release behavior. As shown in Scheme 1, the inorganic backbone of HCCP, composed of N and P atoms arranged by alternating single and double bonds, that can be degraded in biological systems and generate non-toxic products [45]. Moreover, because of high activity of P–Cl bonds and numerous reaction sites of HCCP, all chlorine atoms can be substituted by phenolic hydroxyl groups (-OH) on Cur and form nanospheres (NPs). To improve the water solubility and endow bone-targeting ability of final product, the amino group terminated polyethylene glycol (NH_2-PEG) and alendronate (ALN) were further introduced on the surface of nanoparticles by replacing the remaining P–Cl bonds with amino groups [46]. The water dispersibility, drug release behavior, bone-targeting capability as well as other physicochemical properties of final product HCCP-Cur-PEG-ALN (HCPA NPs) were determined in details. The therapeutic effects of HCPA NPs for OP *in vitro* and in OVX mice were examined. Its mechanism for OP treatment, toxicity and bone-targeting ability *in vivo* were also evaluated and discussed. The results from above experiments confirmed that HCPA NPs are osteoclast inhibitors and osteoblast promoters and effectively reduce bone loss in OVX mice with low toxicity to major organs.

2. Experimental sections

2.1. Materials and characterization

Hexachlorocyclotriphosphazene (HCCP, *M*w = 347.66 Da, 99%), curcumin (Cur, Mw = 347.66 Da, 98%), and alendronate (ALN, *M*w = 325.12 Da, 99%) were obtained from Heowns Reagent Co., Ltd. (Tianjin, China). N, *N*-dimethylformamide (DMF, *M*w: 73.09 Da, 98%) and N, N, *N*-triethylamine (TEA, *M*w: 101.19 Da, 99%) were purchased from Aladdin Reagent Co., Ltd. (Shanghai, China). The following reagents were obtained from Gibco-BRL (USA): alpha modified minimum

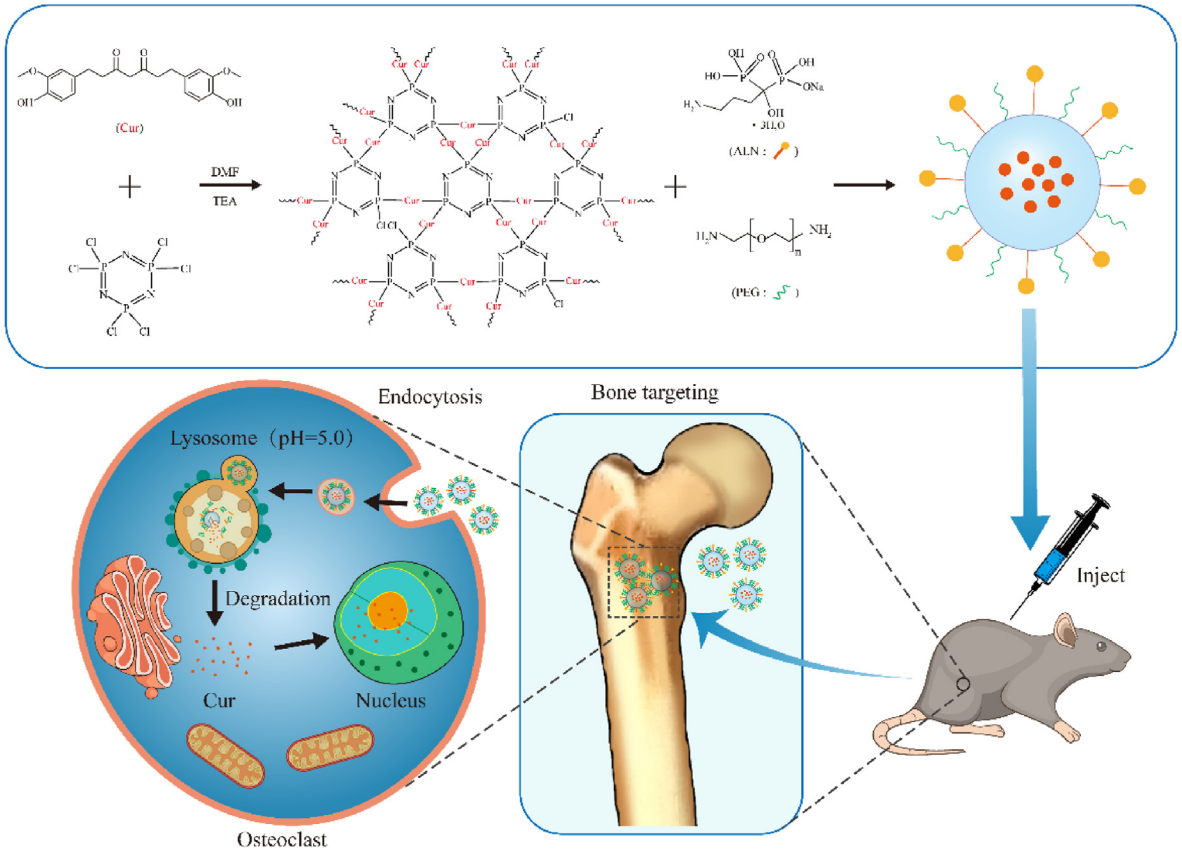

Scheme 1. Schematic synthesis of pH-responsive bone-targeted HCPA NPs based on condensation reaction of Cur, PEG and ALN by using HCCP.

essential medium (α-MEM), high sugar medium DMEM; PBS buffer, fetal bovine serum, and penicillin/streptomycin. Recombinant mouse macrophage colony-stimulating factor (M-CSF) and nuclear factor-κB receptor-activating ligand (RANKL) were purchased from R&D Systems. Other reagents, such as cell counting kit-8 (CCK-8), and anti-tartrate acid phosphatase (TRAP) staining kit, were all purchased from Sigma Aldrich. After the NPs were prepared, a series of instruments, including ^{1}H nuclear magnetic resonance (^{1}H NMR, Bruker Avance-400 spectrometer), Fourier transform infrared spectroscopy (FT-IR, Nicolet 380 Fourier transform spectrometer) spectroscopy, thermogravimetric analysis (TGA), transmission electron microscopy (TEM, Hitachi 7650 B microscope), dynamic light scattering (DLS, ALV/CGS-3 goniometer) and ultraviolet–visible (UV–vis, PerkinElmer Lambda 35) were applied to characterize the products.

2.2. Synthesis of HCP NPs and HCPA NPs

Briefly, the HCCP (34 mg), Cur (60 mg), and NH_2-PEG (30 mg) were respectively dissolved in 10 mL DMF in a 50 mL centrifuge tubes. After that, the tubes were transferred to ultrasound for 5 min to dissolve completely. Following that the dissolved solution was transferred into a 50 mL round reaction bottle and triethylamine TEA (1.5 mL) was added. Herein, TEA acts as both an acid-binding and a catalyst. Ultrasonic irradiation (100 W, 40 kHz) was applied to the reaction for approximately 6 h in an ice bath. As a next step, raw nanoparticles were obtained and transferred to dialysis tubes (3500 Da) to remove incompletely reacted regents and organic solvents. The purification process of products was completed until the dialysis solution was clear and transparent, then freeze-dried to obtain HCP NPs. To further graft ALN on the surface of NPs, the obtained HCP NPs and excessive ALN were respectively dissolved in DMF and deionized water. After that, the solutions were mixed and transferred into the 50 mL round reaction bottle, followed by adding the TEA into the mixtures. Subsequently, the raw products were treated with ultrasonic irradiation (100 W, 40 kHz) for 3 h in an ice bath, followed by two overnight dialysis sessions. Finally, the HCPA NPs were obtained.

2.3. Bone mineral binding ability in vitro

To evaluate the affinity of HCPA NPs to bone tissues, hydroxyapatite (HAp) powders were used as model bone. As described in a previous study [47], HCPA NPs (5 mg) were dissolved in 30 mL PBS solutions, and the maximum absorbance at 425 nm was observed and recorded. After that, 100 mg of HAp was added to the solutions and shaken for 4 h in the dark. Subsequently, the mixtures were sent to centrifuge at 1000 r/min for 5 min, and then the absorbance of supernatant was measured by a UV/vis spectrophotometer at 425 nm. A reduction in percent absorbance at 425 nm represents the binding ratio of HCPA NPs to HAp.

2.4. Drug loading efficiency (DLE) and drug release behavior

First, a standard curve of Cur was obtained before measuring the drug loading capability. The process was described as follows: Cur solutions were prepared in different concentration gradients. The absorbance values at the maximum UV absorption wavelengths (425 nm) of different concentrations of Cur solutions were measured and recorded using a UV–Vis spectrophotometer. After that, the measured values were linearly fitted to the corresponding concentrations of Cur. Then the standard curves of Cur were obtained. Based on it, the DLE of Cur can be calculated as follows: DLE (w/w %) = (weight of loaded Cur/weight of HCPA NPs) × 100%. A further investigation was conducted by dissolving two samples (5 mg each) in PBS solution and transferring them to the dialysis bag (1000 Da). The bags were then immersed in different pH values (5.4 and 7.4) of PBS solution and stirred at 1000 rpm. At each specific time points, 5 mL of dialysate was collected from two groups, and the absorbance at 425 nm was measured and recorded. Then the drug release behavior of Cur was calculated using the formula: Cur released (%) = Ct × V/M. V represents the volume of PBS; Ct represents the concentration of Cur at time t; M represents the total amount of Cur in the dialysis bag.

2.5. Cells and cell culture

Primary monocytes/macrophages (BMMs) of bone marrow were isolated from the femoral and tibial bone marrow cavities of 4- to 6-week-old C57BL/6 mice by washing with complete α-MEM containing 25 ng/mL of M-CSF, 10% fetal bovine serum and 1% penicillin/streptomycin in an incubator at 37 °C, 5% CO_2 for approximately three days, and after adhesion of cells to the wall, they were rinsed with PBS to remove uncoated cells, and the culture medium was replaced. RAW264.7 cells (purchased) were cultured in DMEM containing 10% fetal bovine serum at 37 °C in a 5% CO_2 incubator and passaged every two days.

2.6. In vitro cell viability assay

1×10^4 BMMs cells were inoculated in 96-well plates (purchased) and plastered overnight. Cells were treated with culture medium containing 25 ng/mL M-CSF and different concentrations of HCPA NPs (0, 5, 10, 20, 40, 80, 160, and 320 μg/mL) for 24, 48, and 72 h 10 μL of CCK-8 reagent was added to each well and incubated in incubator for 1 h. The absorbance of each well was then measured at 450 nm using an ELX808 absorbance microplate meter. The absorbance of each well was then measured at 450 nm using an ELX808 absorbance microplate meter. These experiments were repeated three times.

2.7. In vitro cell uptake assay

BMMs cells were inoculated in 96-well plates at 1×10^4 and then incubated in the incubator for 24 h. After cells were plastered, Cur and HCPA NPs were added to the culture medium, and incubation was continued for 24 h. After that, cells were washed with PBS to remove the residual drugs. Cells were subsequently fixed with 4% paraformaldehyde solution for 30 min and then rinsed twice with PBS. Cells were permeabilized with 0.1% (v/v) Triton X-100 for 5 min and then washed with PBS to remove the permeabilization solution. Finally, cells were stained with 20 μg/mL PI solution for 20 min and then washed twice with PBS to remove the residual PI solution. The distribution and intensity of Cur fluorescence signals in each group of cells were observed by laser confocal microscopy. All the above experiments were repeated three times.

2.8. Osteoblast differentiation assay

Briefly, BMMs cells were inoculated in 96-well plates at 1×10^4 and then incubated in the incubator for 24 h. After the cells were plastered, the culture medium containing 25 ng/mL M-CSF, 50 ng/mL RANKL and different concentrations of HCPA NPs (0, 5, 10, 20 μg/mL) was replaced. The cells continued to culture for 5–8 days until mature osteoblasts were formed in the control group. The residual culture medium was removed with PBS before staining, and 4% paraformaldehyde was added to fix the cells for 30 min. Subsequently, the fixative was removed and stained with a TRAP kit. The staining cells were observed under a light microscope and photographed. TRAP-positive cells containing more than or equal to three nuclei in a cell were counted using image j software, and their areas were measured. All the above experiments were repeated three times.

2.9. F-actin ring formation assay

Briefly, BMMs cells were seeded into a 48-well plate and then incubated in a culture medium containing 25 ng/mL M-CSF, 50 ng/mL RANKL and various concentrations of HCPA NPs (0, 5, 10, 20 μg/mL). Cells were continuously cultured until mature osteoblasts formed. Before staining, the residual culture medium was removed with PBS, and cells

were fixed with 4% paraformaldehyde for 30 min. After that, the fixative was removed, and cells were permeabilized with PBS containing 0.1% (v/v) Triton X-100 for 5 min. Then the F-actin rings of the osteoblasts were stained with onychomycosis-tetramethylrhodamine isothiocyanate, and the nucleus was stained with DAPI for 5 min. Finally, staining was observed in an immunofluorescence microscope, and the results were quantified using image j software. The above experiments were repeated three times.

2.10. In vitro bone resorption assay

BMMs cells were inoculated at 1×10^4 on bovine bone slices, and osteoclast was stimulated with culture medium containing M-CSF, RANKL, and various concentrations of HCPA NPs (0, 5, 10, 20 μg/mL). The fluid was changed every two days. After at least nine days, the bovine bone sections were washed with 4% sodium hypochlorite to remove adherent cells from their surface. The formation of bone resorption traps on the bovine bone slices was observed by scanning electron microscopy and quantified by image j software. These experiments were repeated three times.

2.11. RNA extraction and real-time fluorescence quantitative PCR analysis

To examine the effect of HCPA NPs on the mRNA expression level of osteoblasts, BMMS cells were inoculated at 1×10^5 in a 6-well plate and cultured with α-MEM containing 25 ng/mL M-CSF and 50 ng/mL RANKL. After stimulation with 0, 5, 10, and 20 μg of HCPA NPs for five days, cells were lysed with TRIZOL, and total RNA was extracted using RNAiso reagent (Qiagen, Germany). Reverse transcriptase synthesized cDNA using 1 g of total RNA as a template. PCR amplified the cDNA. After electrophoresis on 1% agarose gels, PCR products were photographed using the ImageQuant LAS 4000 Documentation System (GE Healthcare). Furthermore, ABI 7500 Sequencing Detection System (Applied Biosystems) and SYBR Premix Ex Tag Kit (TaKaRa) were used for quantitative real-time PCR.

2.12. Protein extraction and immunoblotting

The effect of HCPA NPs on the initiation of RANKL-induced osteoclastogenesis was studied using a protein immunoblotting technique. First, RAW264.7 cells were inoculated in six-well plates at 5×10^5. When the cells grew to a density of about 70% of the total plate area, 50 ng/mL RANKL alone or co-stimulated with 20 μg/mL HCPA NPs was added and incubated for 0, 1, and 3 days. To extract total cellular proteins, cells were washed twice with PBS and lysed with RIPA lysate containing protease/phosphatase inhibitors to release intracellular proteins. The lysate was then centrifuged in a four-degree centrifuge at $12{,}000 \times g$ centrifugal force for 15 min to remove the cellular sediment. The supernatant was collected for protein quantification by bicinchoninic acid colorimetric assay (BCA). Protein samples were separated by electrophoresis and transferred to PVDF membranes. The PVDF membrane was blocked with 5% skim milk for 1.5 h at room temperature and washed three times in Tris-Buffer saline containing 1% Tween. The membrane was then incubated with the specific primary antibody overnight at 4 °C. The membranes were washed three times again with Tris-Buffer saline, and RaMIgG-HRP was added and incubated at room temperature for 1.5 h. Chemiluminescence detection system detected the density of specific bands of osteoclast-associated proteins and quantified them using image j software. These experiments were repeated three times.

2.13. In vivo bone targeting efficiency of HCPA NPs

Experiments were performed using athymic female nude mice (5–6 weeks). Mice were randomly divided into three groups: control, Cur, and HCPA NPs groups. Equal volumes of PBS, Cur solution, and HCPA NPs solution were administered to three groups of mice by intraperitoneal injection. The *in vivo* fluorescence imaging signals of mice were collected using 440/530 nm filters after 0, 6, and 12 h of drug injection to take advantage of the properties of Cur-containing fluorophores. A 12 h after drug administration, mice were euthanized with 1% pentobarbital. The internal organs of mice were quickly dissected, and the fluorescence imaging signals of each organ were collected at this time. The collected fluorescence signal intensity was quantified using IVIS Lumina XR (Caliper Life Sciences Inc., MA, USA).

2.14. Establishment of a mouse model of bone loss after ovariectomy (OVX)

Thirty 6–8-week-old female C57BL/6 mice were purchased from Changsha Tianqin Biotechnology Co. Mice were housed in a temperature-controlled environment at 22–25 °C and 60% ± 5% humidity and given standard rodent chow and an adequate supply of fresh water. After one week of acclimation, the above 30 mice were randomly divided into five groups: sham-operated group, OVX group (vehicle group), OVX + Cur group, OVX + low-dose HCPA NPs group (7.2 mg/kg), and OVX + high-dose HCPA NPs group (14.4 mg/kg). The ovariectomy procedure was as follows: mice were anesthetized with 10% chloral hydrate, hair was shaved on the back of the mice, and after skin preparation was completed, an incision of approximately 1 cm was made on the lateral edge of the bilateral dorsal spinal muscles, the posterior peritoneum was explored inward and incised, and after the bilateral ovaries were found, the fallopian tubes and ovarian vessels connected with them were ligated smoothly, and the bilateral ovaries and the surrounding adipose tissue were excised (The sham surgery group did not perform tubal ligation, only removing adipose tissue around the bilateral ovaries without damaging the ovarian parenchyma). After one week of postoperative recovery, the mice were injected intraperitoneally with an interval of two days between doses. After two months of continuous administration, blood was collected from the eyes of mice for routine blood tests and liver and kidney functions. All mice were euthanized by injection of 1% pentobarbital. The intact tissues of the femur, tibia, heart, liver, spleen, lung, and kidney organs of mice were isolated and soaked in 4% paraformaldehyde fixative for 24 h and then transferred to 70% ethanol solution for preservation. The Research Ethics Committee of the First Affiliated Hospital of Nanchang University approved all animal experiments and operations.

2.15. Micro-computed tomography (Micro-CT) scan

The left distal femur was scanned with high-resolution Micro-CT, and the femoral structure was reconstructed in three dimensions to quantify the area 0.5 mm below the femoral growth plate. Morphological parameters analyzed for quantification included bone volume fraction percentage (BV/TV; %), trabecular number (Tb. N; mm^{-1}), trabecular thickness (Tb. Th; mm), and trabecular separation (Tb. Sp; mm).

2.16. Histological staining and evaluation

Fixed tibiae were decalcified in 10% EDTA for two weeks, and the tissue was then embedded in paraffin wax and cut into 5-μm-thick sections. The viscera of mice were fixed and then directly sectioned with paraffin-embedded sections. Hematoxylin and eosin (H&E) staining was performed on the tibial and visceral sections. TRAP activity staining was performed in tibial sections, and the number of TRAP-positive polynuclear cells per unit of bone surface area was quantified using image j software.

2.17. Statistical analysis

The statistical analysis results were expressed as mean + SD. Data were analyzed using a one-way ANOVA. Statistically significant was denoted as *, $p < 0.05$; **, $p < 0.01$; and ***, $p < 0.001$.

3. Results and discussion

3.1. Characterization of HCPA NPs

The chemical structure as well as morphology of HCPA NPs and related samples were characterized by NMR, FT-IR, DLS and TEM. Firstly, the ^{1}H NMR spectrum of PEG-NH_2 was shown in Fig S1, the results confirmed the successful synthesis of PEG-NH_2. Fig. 1A shows the ^{1}H NMR spectrum of HCPA NPs. A sharp peak at 2.5 ppm was ascribed to the solvent (DMSO-d_6). Meanwhile, multiple peaks between 7 and 8 ppm were attributed to chemical shifts of *C*–H in conjugated benzene, which should be originated from Cur and suggested the successful conjugated Cur with HCCP. Moreover, the peaks around 3.5 ppm that can be assigned to the *C*–H of ether in PEG, indicating that PEG has also successfully grafted on the surface of HCPA NPs. Furthermore, the small peak near 3 ppm belongs to the characteristic peak of methylene, indicating successful grafting of ALN onto HCPA NPs. FT-IR spectroscopy was further performed to characterize the chemical information and functional groups of the samples and results are shown in Fig. 1B. For example, at characteristic peaks at 1166 cm^{-1} and 831 cm^{-1} are corresponded to stretching vibrations of P═N and P–N, respectively. And the characteristic absorption peaks at 1509 cm^{-1} and 1618 cm^{-1} were assigned to vibrations of C═C (ph). Moreover, stretching vibrations at 935 cm^{-1} and 656 cm^{-1} were respectively attributed to the stretching vibration bond of P–O and P═O from phosphate. Furthermore, the peak at 1262 cm^{-1} was attributed to ether bonds (*C*–*O*–C). More importantly, compared to the FT-IR spectrum of HCCP, the characteristic peak of P–Cl bond at 601 cm^{-1} was disappeared and new peaks at 1053 cm^{-1} and 967 cm^{-1}, respectively related to stretching vibration bonds of P–N–C and P–*O*-(ph) were appeared in the FT-IR spectra of HCPA NPs. The above comparison and changes clearly demonstrated that chlorine atoms of HCCP have been successfully replaced by phenolic groups of Cur, and amino groups of PEG or ALN. In other word, we have successfully constructed HCPA NPs via using HCCP as the linkage. The particle size plays an essential role in for drug delivery systems [48]. It was reported that nanoparticles with particle size between 50 and 200 nm were reported to exhibit enhanced cellular uptake [49]. Thus, in the following section, the particle size of HCPA NPs was measured by DLS and TEM. The results showed that the average size of HCPA NPs was 181.9 ± 25.9 nm with polydispersity index (PDI) of 0.206 (Fig. 1C). Besides, the hydrodynamic size of HPCA NPs in cell culture medium was also measured. As shown in Fig. S2, the size of HPCA NPs was determined to be 193.7 ± 46.3 nm with PDI of 0.188. The TEM was performed to further investigate the size and morphological characteristics of HCPA NPs. Fig. 1D reveals that spherical NPs with an average diameter of 150 nm were observed. The particle size of HCPA NPs measured by TEM is well consistent but slightly smaller than that measured by DLS. It can be attributed to the hydration shell surrounding the particles [50]. Furthermore, Zeta potential (ZP) is another key factor for evaluating the stability of NPs dispersion, the ZP value of HCPA NPs in PBS solution (pH = 7.4) was determined to be −29.6 mV, indicating the good suspension stability of HCPA NPs [51].

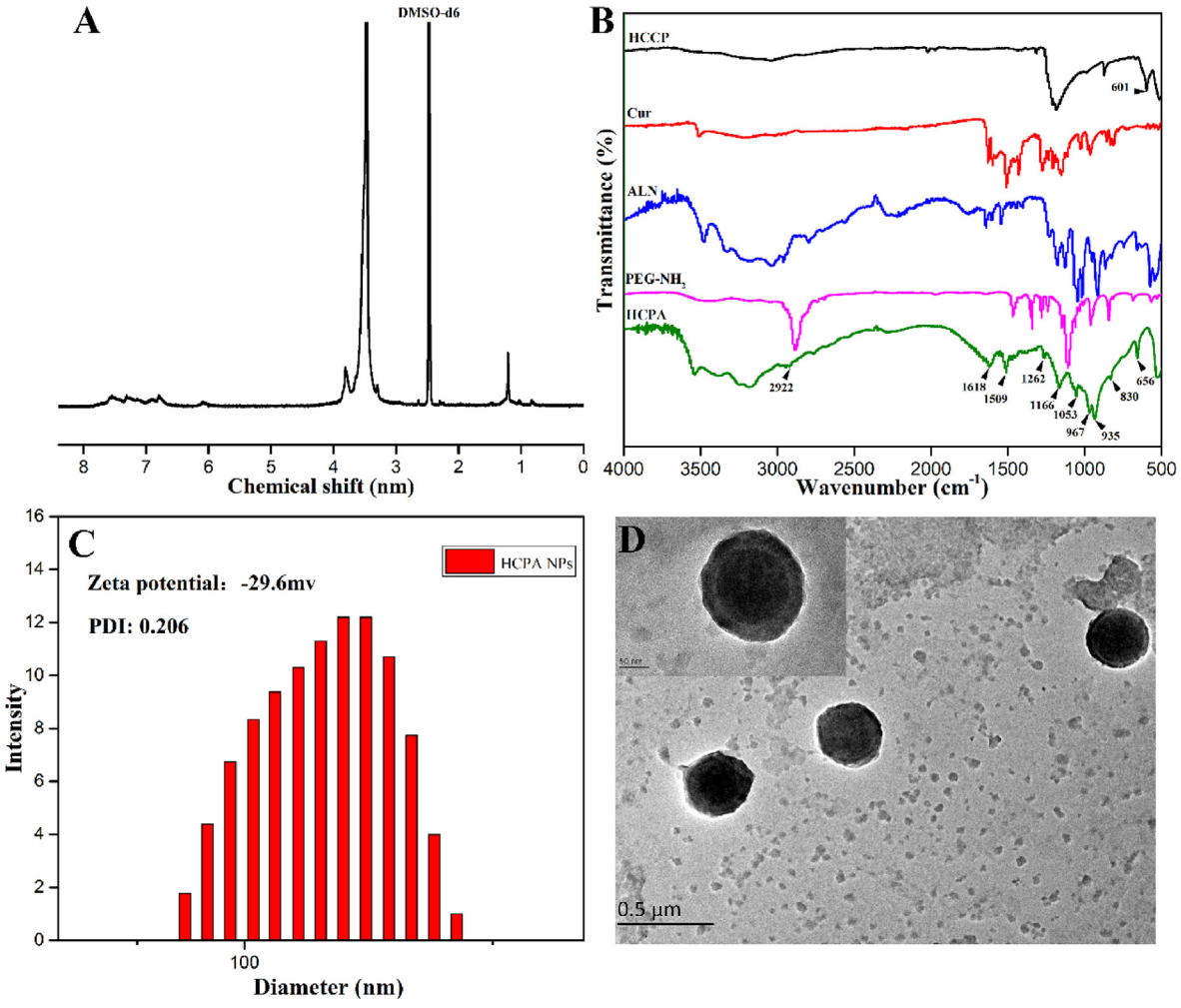

Fig. 1. (A) ^{1}H NMR spectrum of HCPA NPs; (B) FT-IR spectra of HCPA NPs; (C) DLS of HCPA NPs; (D) TEM image of HCPA NPs.

3.2. Drug loading capability and release behavior

As an ideal formulation, satisfactory drug loading capacity and controlled drug release were the two key factors for drug delivery [52]. High drug loading capacity may reduce metabolic stress on the liver and kidney, while the controlled release of drugs may reduce drug loss during transport [53]. In this study, we used the UV–vis spectrum to calculate the load of Cur on the HCPA NPs. Fig. 2A is the standard curve of Cur based on the UV–Vis absorbance at 425 nm, the results suggested that the absorbance and concentrations of Cur shows a good linear relationship with a Pearson correlation coefficient of 0.9991. According to the standard curve, the loading capacity of Cur on HCPA NPs was calculated to be 25.8 w/w %, which is higher than other drug delivery systems [54–56]. Because the P–O bonds between HCCP and Cur can be broken under acidic environment, we measured the release behavior of Cur from HCPA NPs in PBS solution with different pH values (pH = 5.4 and pH = 7.4, respectively). As shown in Fig. 2B, we found that the Cur is rapidly released from HCPA NPs during the first 7 h both in pH = 5.4 and pH = 7.4 solution. This is possibly ascribed to the higher concentration gradient between the inner and outer solutions. However, the release rate gradually decreased in the solution of pH = 7.4 and remained at 30.6% after 60 h, while relative fast drug release behavior can be found in the solution of pH = 5.5 and the total release rate can reach to 60.9%. The possible reason is the higher breakage speed of P–O bonds under acidic environment [57]. These above results proved that HCPA NPs have high loading capability and Cur can be controlled release from HCPA NPs with pH responsiveness, which is promising for intracellular delivery of bioactive molecules and avoiding their toxic side effects.

3.3. Bone targeting efficiency of HCPA NPs and HCP NPs

As the main ingredient of bone, hydroxyapatite is a unique mineral and useful target for developing bone-targeting drug delivery systems [58]. In this study, ALN was used as a bone-targeting ligand with high affinity to hydroxyapatite in the bone matrix due to its molecular structure containing two phosphate groups [47]. Fig. 2C and D are the comparison binding ability of HCP NPs and HCPA NPs towards hydroxyapatite. After mixing HCP NPs and HCPA NPs with hydroxyapatite in the same experiment conditions, we found that there are 54.4% HCPA NPs and 36.1% HCP NPs were adsorbed by hydroxyapatite. The above comparison indicated that HCPA NPs are surely of bone-targeting property.

3.4. Cellular uptake and intracellular distribution of HCPA NPs

Before nanoparticles can enter the cells to play a biological role, they must overcome cellular permeability. Cur is well known to go through the lipid bilayer of cell membrane by free diffusion to exert its biological effects [59]. Owing to its small size (181.9 ± 25.9 nm), HCPA NPs might be effectively ingested into the cell by endocytosis [60]. To test this hypothesis, we used the fluorescence microscopy to investigate the intracellular distribution of HCPA NPs by taking advantaging of the

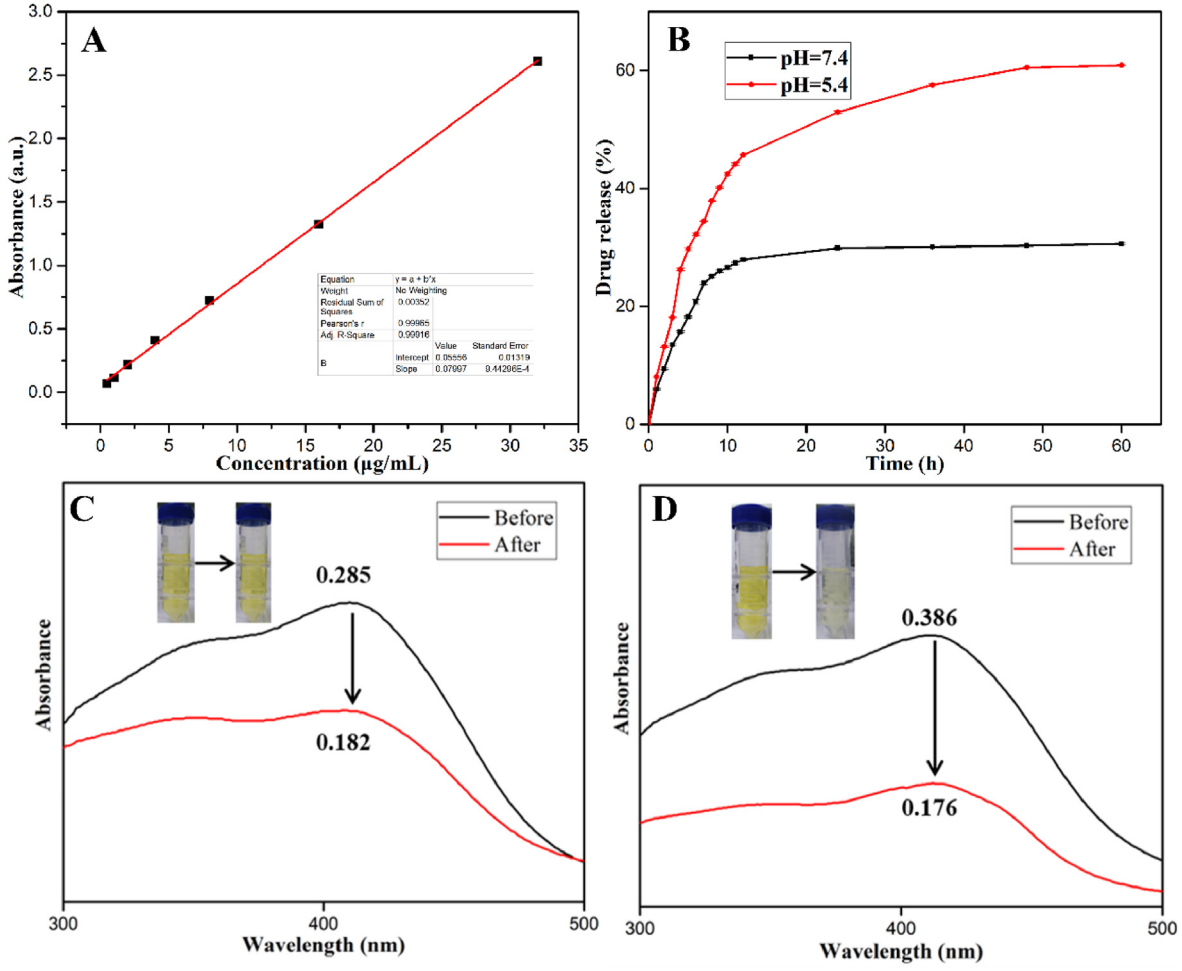

Fig. 2. (A)The standard curve of Cur obtained by UV spectrophotometry at a wavelength of 425 nm wavelength; (B) drug release behavior of HCPA NPs at pH = 5.4 and pH = 7.4; the bone mineral binding ability of HCP NPs (C) compared to HCPA NPs (D).

autofluorescence of Cur. Before that, the excitation and emission fluorescence spectra of HCPA NPs were measured (shown in Fig. S3). And the maximum excitation wavelength and maximum emission wavelength of HCPA NPs are around 430 and 540 nm, respectively. As shown in Fig. 3A, after incubation of BMMs with free Cur and HCPA NPs, green fluorescence signals appeared in cells in both experimental groups, which is well consistent with the fluorescence locations dyed by PI. The above results demonstrated that HCPA NPs are efficiently internalized by osteoclasts without affecting Cur transport efficiency. Following our scenario, the NPs internalized by the cells are transported to the lysosomes in the form of vesicular trafficking and are decomposed for releasing Cur into the cytoplasm in the acidic environment of lysosomes. The free Cur in the cytoplasm then crosses the barrier of nucleus membrane by simple diffusion. Finally, it exerts its role in inhibiting the formation and differentiation of osteoclasts in the nucleus.

3.5. Inhibition of osteoclast function by HCPA NPs in vitro

With any medication, the concentrations must be maintained within a therapeutic window in which the drug is efficacious and safe. In the following section, we examined the cytotoxic effects of HCPA NPs on RAW264.7 and BMMS to assess the safe concentration range for HCPA NPs. The CCK-8 assay indicated that cell death begins only after the incubation concentration of HCPA NPs is greater than 40 μg/mL (Fig. 3B). Based on cell survival curves in Fig. 3B, The IC50 values of HCPA NPs towards RAW264.7 and BMMS were calculated to be 62.15 and 67.61 μg/mL, respectively after 72 h of exposure. The above results reveal that HCPA NPs are biocompatible enough in a wide range of concentrations. By using a non-toxic concentration of HCPA NPs, we evaluated its effect on osteoclast production. BMMs, as precursor cells of osteoclasts, are stimulated by a colony-stimulating factor (M-CSF) and nuclear factor receptor activator kB ligand (RANKL), in which mononuclear BMMs fuse with each other to form multinucleated giant cells and after further integration and cytoskeletal rearrangement differentiate into osteoclasts. Tartrate-resistant acid phosphatase (TRAP) is the signature enzyme of mature osteoclasts and osteoclast-derived growth factor commonly identified as osteoclast [61–63]. We measured osteoclastogenesis by calculating the number of TRAP-positive cells with more than three nuclei and their occupied area. The results showed that the number and surface of osteoclasts formed in the dish after RANKL stimulation alone were large. However, after RANKL co-incubation with different concentrations of HCPA NPs, the number and the surface of osteoclasts formed in the dish decreased with increasing HCPA NPs concentration (Fig. 3C and D). This indicated that HCPA NPs dose-dependently inhibit RANKL-induced osteoclast formation. The volume and number of osteoclast nuclei are closely related to their bone resorption activity, so the above results suggest that HCPA NPs affect osteoclastic bone resorption.

To further explore whether HCPA NPs affect the bone resorption function of osteoclasts, we performed osteoclast F-actin ring and bone resorption lacunae detection. During bone resorption, osteoclasts

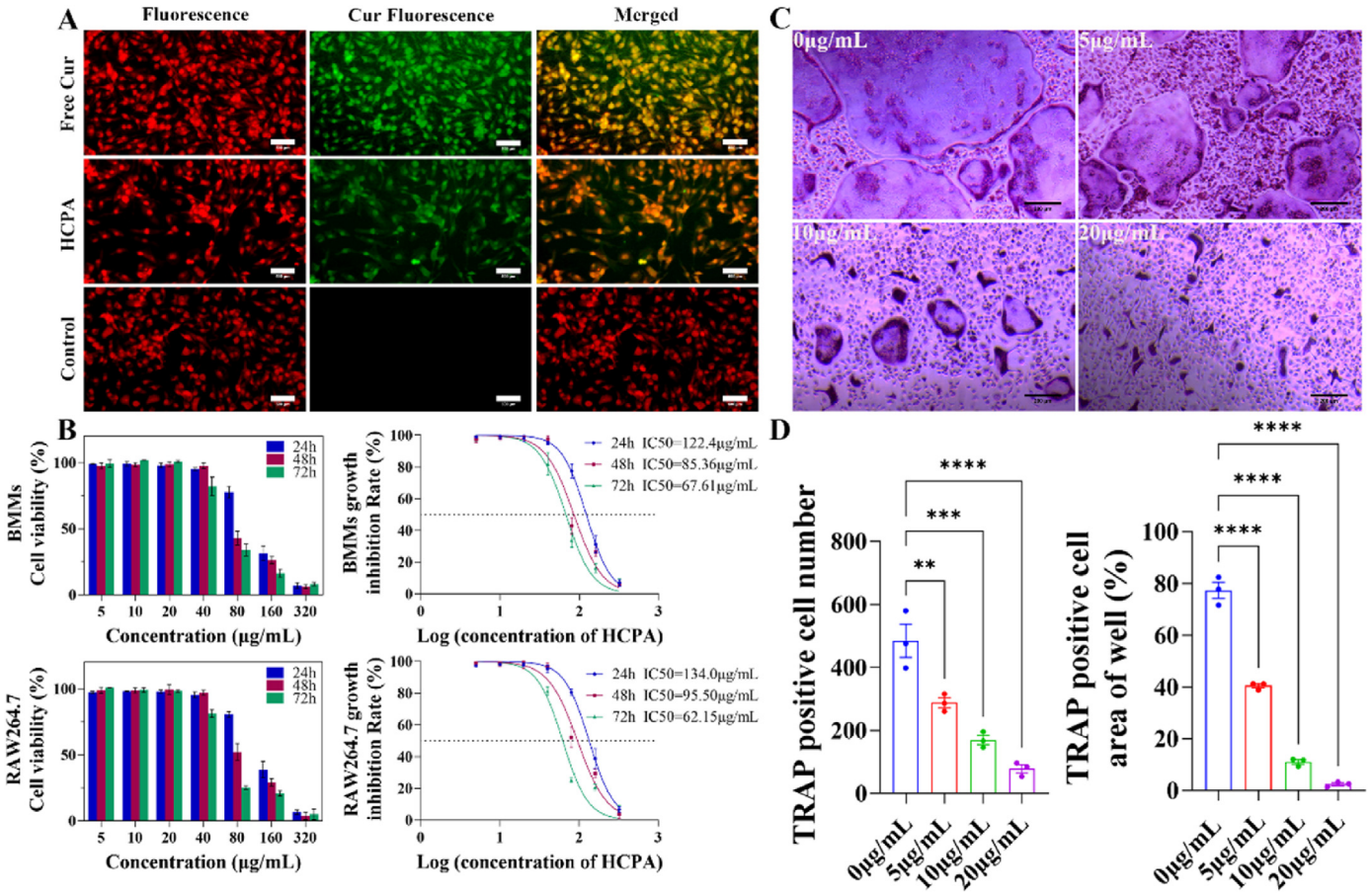

Fig. 3. HCPA NPs internalized by cells and inhibit RANKL-induced osteoclastogenesis *in vitro* in a dose-dependent manner without cytotoxicity. (A) Intracellular localization of HCPA NPs (red: nucleus; green: Cur). Scale bar = 500 μm; (B) cell survival rate and cell survival curve of bone marrow monocyte/macrophage cells (BMMs) and RAW264.7 cells after 24, 48, and 72 h treatment with different concentrations of HCPA NPs; (C–D) the number and area percentage of tartrate-resistant acid phosphatase (TRAP)-positive multinucleated osteoclasts were determined after the BMMS were cultured in medium containing different concentrations of HCPA NPs for 5–8 days. Scale bar = 200 μm. (All data are expressed as mean ± standard error. *$p < 0.05$, **$p < 0.01$, ***$p < 0.001$ and ****$p < 0.0001$; ns indicates no significant difference). (For interpretation of the references to colour in this figure legend, the reader is referred to the Web version of this article.)

reorganize the actin cytoskeleton and cell polarization, forming a distinctive apical membrane (towards the bone surface) and a basolateral membrane domain (away from the bone surface). The region towards the bone surface is called the ruffled border, surrounded by an abundance of actin. The actin ring anchors osteoclasts to a mineralized matrix, forming a bone resorption cavity within which bone resorption functions are performed [64]. Given the important role of actin ring in osteoclast migration and bone resorption, it is considered a functional biomarker of osteoclast activation. We performed immunofluorescence analysis to detect F-actin expression in the cultured BMMs, Fig. 4A and B illustrate that the surface area of F-actin ring becomes smaller, and the number of intact F-actin ring decreases with the increasing concentrations of HCPA NPs. We speculate that HCPA NPs can inhibit osteoclastic actin ring formation and thus inhibit bone resorption. After osteoclasts are anchored on the bone matrix surface, HCl and various proteolytic enzymes are actively secreted into the bone absorption cavity through the ruffled border, decomposing organic matter and inorganic minerals on the bone matrix surface and then releasing the breakdown products into the blood. Fig. 4C and D illustrate that osteoclasts were planted on bovine bone slices and observed by scanning electron microscopy (SEM) for bone uptake after the engagement of HCPA NPs. We found that the size and number of bone resorption pits on bovine bone slices decreased significantly as the concentrations of HCPA NPs increased, which further confirmed that HCPA NPs can effectively inhibit osteoclast-mediated bone resorption. This effect is attributed, at least partially, to the inhibitory effect of HCPA NPs on F-actin ring formation.

In the following section, we further investigated the effect of HCPA NPs on osteoclast gene expression. During osteoclast differentiation and activation, RANKL-induced signaling pathways, including the MAPK, NF-kB, and PI3K-AKT signaling pathways, trigger the expression of transcription factors and downstream osteoclast-specific genes [65–67]. Therefore, the inhibition of RANKL-mediated osteoclast signaling axis is a potential strategy for OP treatment. RT-PCR showed that stimulation of RAW264.7 b y RANKL significantly up-regulated the expression of genes that encode osteoclast formation and differentiation compared to the control group (Fig. 5A–E). Among these genes, DC-STAMP, a dendritic cell-specific transmembrane protein, a seven-fold transmembrane protein that is directly involved in the regulation of cell-to-cell fusion, and it is also commonly used as a marker of osteoclast fusion [68]. c-Fos and NFATc1 are the key nuclear transcription factors in osteoclast differentiation [69,70]. The heterodimer transcription factor AP-1 consists of c-Fos/c-Jun increased NFATc1 expression and transcriptional activity

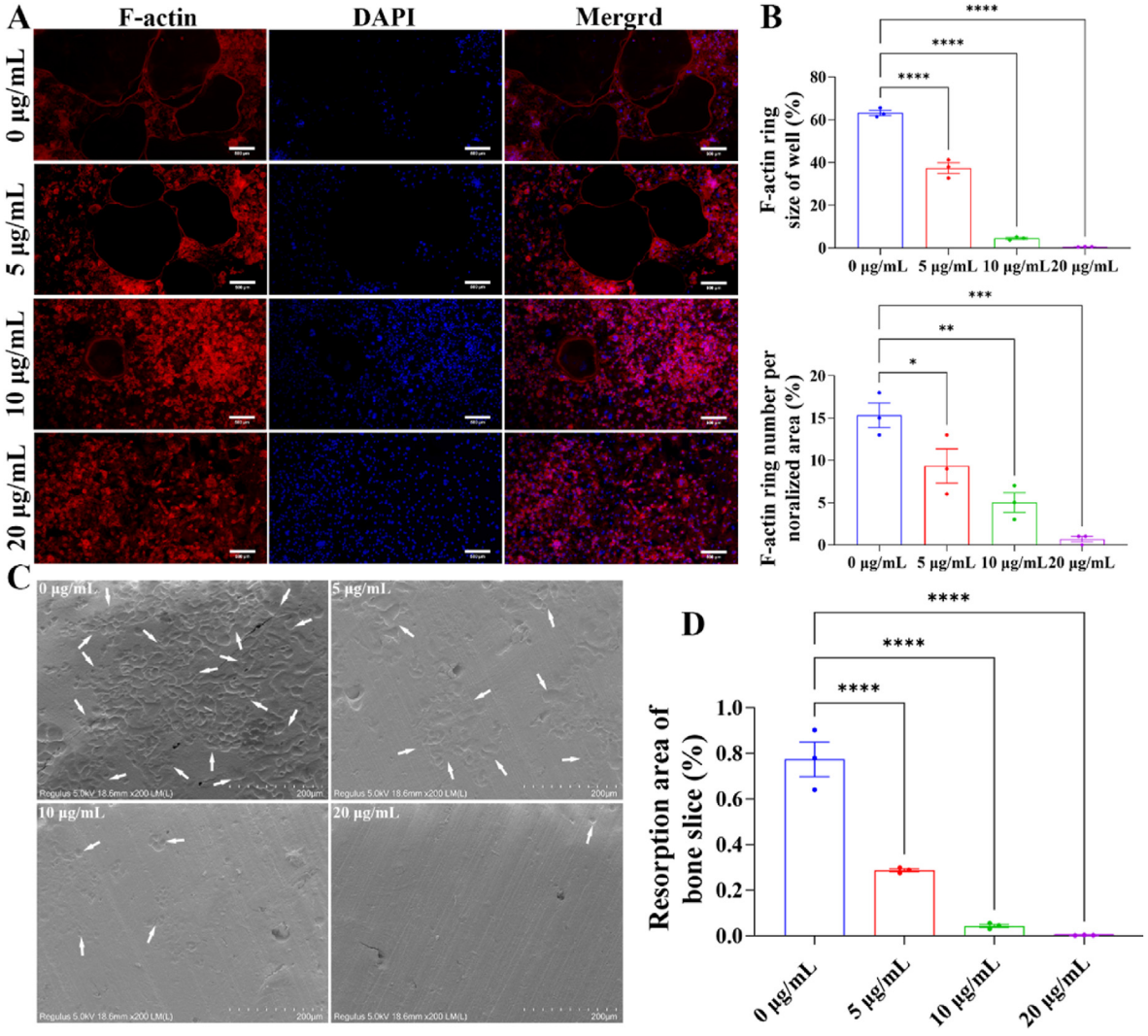

Fig. 4. HCPA NPs inhibit the differentiation and bone resorption function of osteoclasts *in vitro*. (A–B) BMMs were cultured in a medium containing different concentrations of HCPA NPs for 5–8 days, and the size and number of F-actin rings were detected. Scale bar = 500 μm; (C–D) BMMs were cultured in a medium containing different concentrations of HCPA NPs for 5–8 days, and the area of bone resorption pits on bovine bone slices was detected. Scale bar = 200 μm. (All data are expressed as mean ± standard error. *$p < 0.05$, **$p < 0.01$, ***$p < 0.001$ and ****$p < 0.0001$; ns indicates no significant difference).

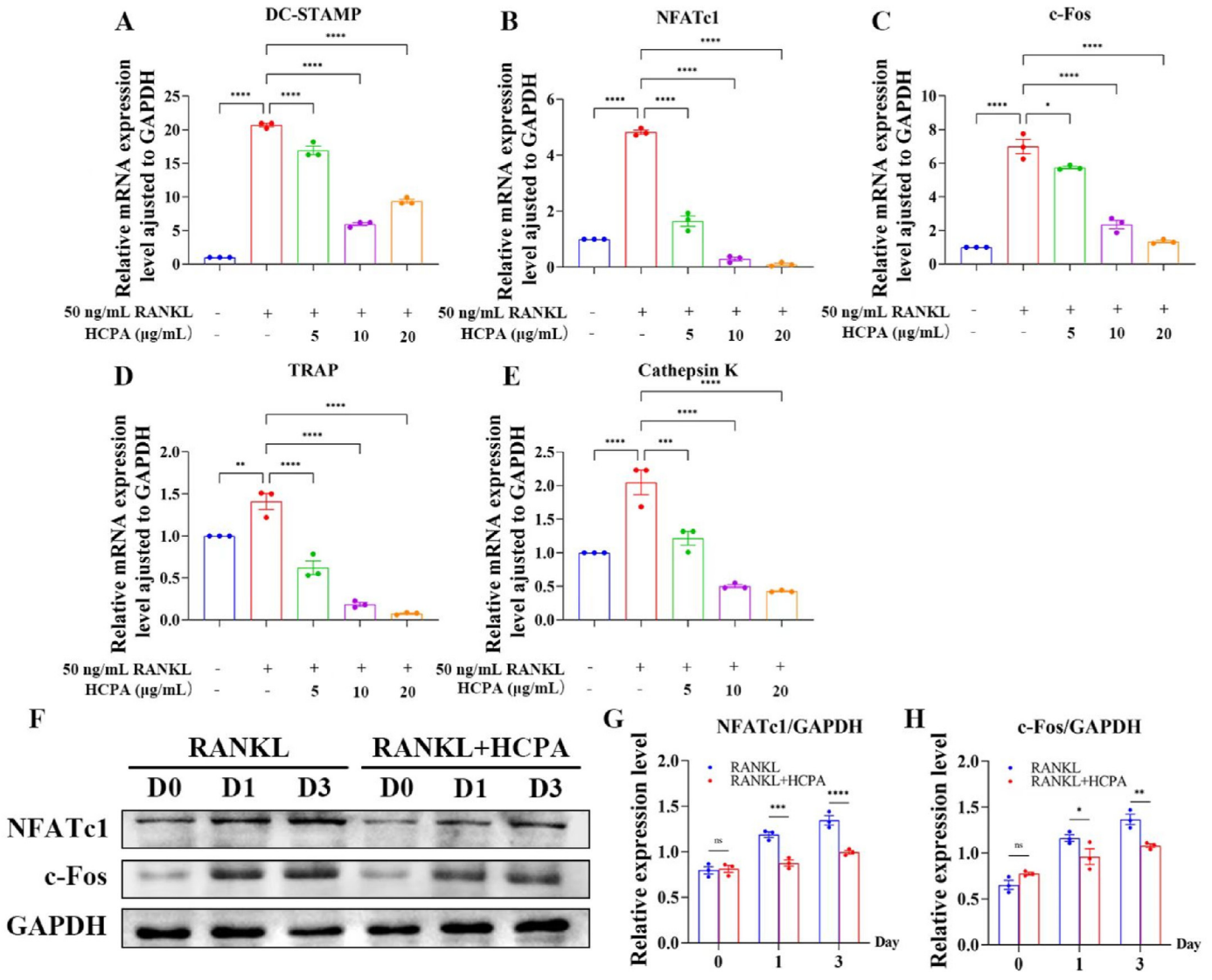

Fig. 5. HCPA NPs downregulate RANKL-induced osteoclast-specific gene expression. (A–E) We cultured BMMs with M-CSF (25 ng/mL), RANKL (50 ng/mL), and HCPA NPs (0, 5, 10, or 20 μg/mL) for five days, and then total RNA was extracted and quantified by quantitative PCR to detect mRNA expressions of TRAP, Cathepsin K, DC-STAMP, c-Fos, and NFATc1; (F–H) we cultured RAW264.7 with RANKL (50 ng/mL) and HCPA NPs (0 or 20 μg/mL) for 0 , 1 or 3 days. Western blot extracted and quantified the total protein to detect protein expressions of c-Fos and NFATc1. (All data are expressed as mean ± standard error. *$p < 0.05$, **$p < 0.01$, ***$p < 0.001$ and ****$p < 0.0001$; ns indicates no significant difference).

[71]. Up-regulated expression of NFATc1 induces the expression of various osteoclast-specific genes, including TRAP, MMP9, and cathepsin K, which encode enzymes that produce osteoclast bone resorption [72]. When cells co-incubated with HCPA NPs, it is observed the decrease expression of the above genes in RAW264.7 with the increase concentrations of HCPA NPs (Fig. 5A–E). Therefore, it is reasonable to believe that HCPA NPs can inhibit RANKL-mediated osteoclastic formation and differentiation, reduce osteoclasts to produce bone resorption-related proteins, and thereby inhibit osteoclastic bone resorption. This inhibitory effects of HCPA NPs on osteoclast activation-related signaling pathways such as NF-κB or the MAPK signaling pathway were further investigated. The protein expression was determined by Western blot analysis after RAW264.7 was treated with RANKL and HCPA NP for 0, 1, and 3 days. The results showed that HCPA NPs could partially inhibit RANKL-induced NFATc1 and c-Fos protein expression. (Fig. 5F–H). This indicates that HCPA NPs inhibit the differentiation and maturation of osteoclast from the early stage of its development and exert a sustained inhibitory effect until the middle and late stages of osteoclast development, the expression of proteins related to cell differentiation detected in osteoclasts remains at a low level. Based on the above results, we can confirm that HCPA NPs can effectively inhibit the synthesis of osteoclast activating factors in the early transcription or translation stage, thus affecting the normal differentiation and fusion of osteoclasts, and inhibiting the secretion of related proteolytic enzymes. This finding may lead to additional insights into the drugs' mechanisms of action.

3.6. *In vivo imaging and biodistribution of HCPA NPs*

To understand the distribution, metabolism, and excretion of HCPA NPs in organisms, the fluorescence signal intensity of samples in nude mice after 12 h intraperitoneal injection was determined. Fig. 6A shows that after 6 h intraperitoneal injection of Cur or HCPA NPs, the fluorescence signal was observed over the body of nude mice. With the observation time extended to 12 h, the fluorescence signal intensity was significantly weakened. The possible reason is the drug metabolism in the liver of mice and excretion by the kidneys and intestines. However, as compared with the fluorescence image of Cur, the fluorescence intensity of HCPA NPs is obvious stronger (Fig. 6A). The difference distribution

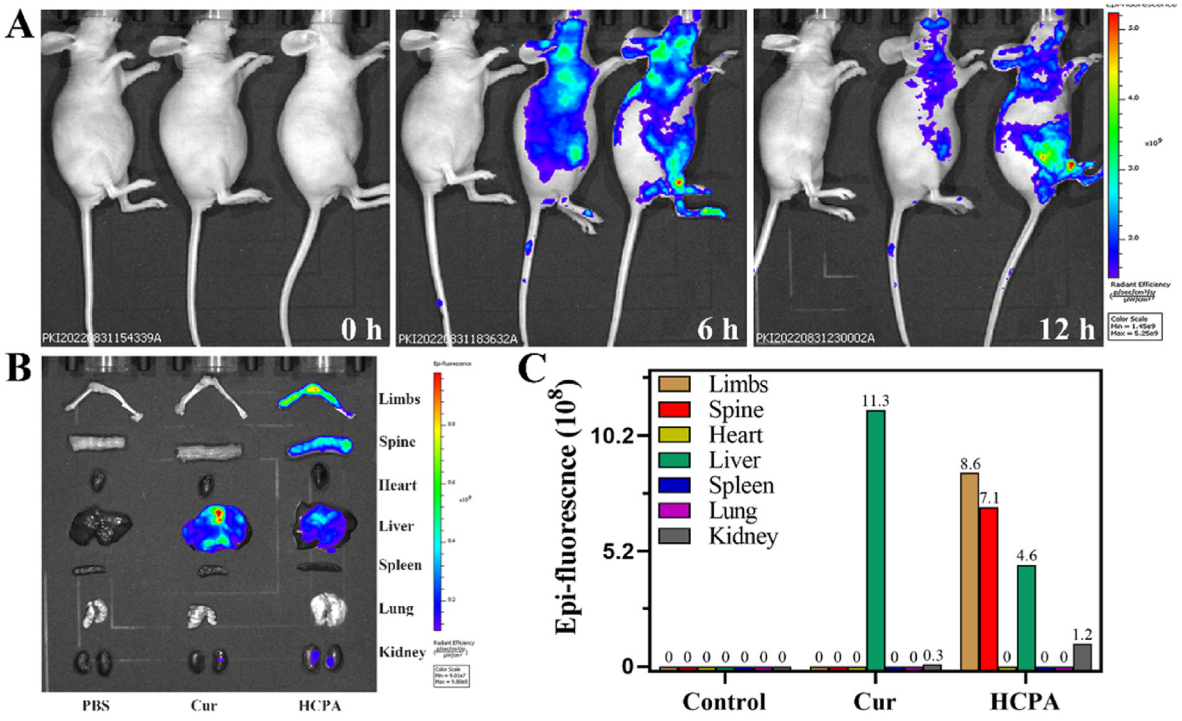

Fig. 6. *In vivo* biodistribution of HCPA NPs using fluorescence imaging (A) distribution of fluorescence signal over time after intraperitoneal injection of PBS, Cur, and HCPA NPs in nude mice; (B) fluorescence imaging of major organs and bones of nude mice after 12 h intraperitoneal injection; (C) statistical analysis of the relative fluorescence intensity of major organs and bones.

behavior can be ascribed to the relative larger particle size of HCPA NPs than Cur, making HCPA NPs in blood circulation difficult to be excreted from the kidneys. Another reason is PEG segment in HCPA NPs has a stealth surface, allowing HCPA NPs to avoid being recognized and cleared by the reticuloendothelial system (RES). The above factors endow HCPA NPs higher effective blood concentrations and long blood-circulation time. It is worth to note that the fluorescence intensity of HCPA NPs at hind leg of mice is also significant stronger than that of Cur. This can be explained by the bone-targeting capability of HCPA NPs owing to the existence of ALN on the surface of HCPA NPs. The tissue-selective distribution of HCPA NPs increases the effective concentration of drug in the target tissue while reducing the circulating drug concentration, thereby helping to reduce the toxic side effects of drug on other tissues and organs. Moreover, after the nanomedicine was accumulated the targeted sites, the bioactive compounds, such as Cur and ALN were released after phagocytosed by osteoclasts. It is therefore, ALN can directly promote the apoptosis of mature osteoclasts on the bone surface, while Cur could also exert its activity to inhibit the differentiation and maturation of osteoclasts. To better understand the bone-targeting capability of HCPA NPs, the fluorescence signals in various organs after administration of Cur and HCPA NPs for 12 h were determined. As displayed in Fig. 6B, Cur is majorly distributed in liver with a small part in kidney after 12 h injection. This suggested that Cur will be absorbed after intraperitoneal injection and mainly accumulated in liver. Obviously different from the distribution results of Cur, we observed strong fluorescence signals in limbs and spine after injection of HCPA NPs and relative weak fluorescence in liver and kidney. The difference distribution behavior further implied that HCPA NPs have ascertain bone-targeting ability for the suitable size and phosphate groups on its surface. The detailed distribution information about Cur and HCPA NPs in different organs was quantitatively analyzed based on the fluorescence intensity of internal organs. We can see that the relative fluorescence intensity of Cur in liver in Cur group was significantly higher than that in HCPA NPs group, while strong fluorescence signals in the spine and limbs were observed in HCPA NPs group (Fig. 6C). It should be illustrated that the fluorescence signals in kidney in Cur group is weaker than that in HCPA NPs group. This is most likely due to the rapid accumulation of Cur in RES and fast excretion of Cur from kidney after Cur was absorbed into blood. Based on the distribution results of Cur and HCPA NPs, we can conclude that the formation of HCPA NPs can not only improve the water dispersibility of Cur and greatly prolong the blood circulation time of nanomedicine, but also avoid the accumulation in RES and enhance the local drug concentration in targeted organs. More importantly, Cur can be released from HCPA NPs after cell endocytosis and exert its biological activity for OP treatment. Given its high water dispersibility, low toxicity, excellent bone targeting capability and acid-triggering intracellular release, we can expect that HCPA NPs will be a promising nanomedicine for OP treatment because it can elegantly overcome the issues of Cur, such as poor dispersibility, whole body distribution, short circulation time and potential side effects to non-targeted organs.

3.7. *In vivo* biological evaluation of HCPA NPs

To further verify above hypothesis, therapeutic effects of HCPA NPs in treatment of OP *in vivo* were examined. By resecting both ovaries of C57BL/6 mice, a model of estrogen deficiency-induced OP was constructed. Here, we evaluate the impact of HCPA NPs on preventing bone loss *in vivo* by comparing femoral morphological parameters. After two months of treatment, Micro-CT scans of the left distal femur of five groups were shown in Fig. 7A. As compared to the sham group, the bone parameters of the mice in the OVX group changed significantly and indicated severe bone loss. This means that the estrogen deficiency-induced bone loss model has been successfully constructed. Based on this model, we studied the protective effect of Cur on bone loss. Consistent with previous studies, trabecular volume was preserved in OVX + Cur group. Better therapeutic effects can be found in OVX + HCPA groups with low and high dosages as compared with the OVX + Cur group. The quantitative bone parameters showed that bone volume compared to total tissue volume (BV/TV), trabecular number (Tb. N), and trabecular thickness (Tb. Th) increased accompanied by Trabecular

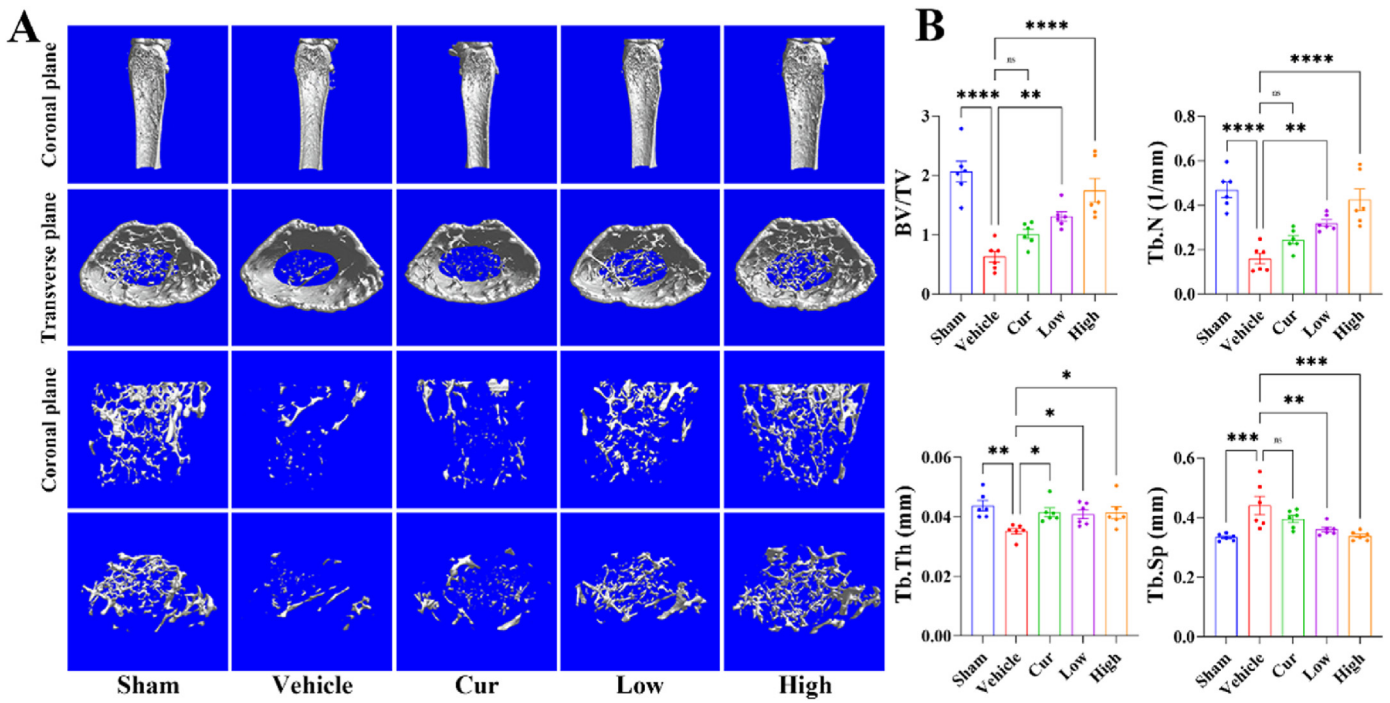

Fig. 7. Evaluation of the efficacy of HCPA NPs in ovariectomized mice (OVX). (A–B) The distal femur of each group of mice after surgery eight weeks for 3D reconstruction, and bone volume relative to total tissue volume (Bv/Tv), Trabecular Number (Tb. N), Trabecular Thickness (Tb. Th) and Trabecular Separation/Spacing (Tb. SP) were measured (All data are expressed as mean ± standard error. *p < 0.05, **p < 0.01, ***p < 0.001 and ****p < 0.0001; ns indicates no significant difference).

Separation/Spacing (Tb. Sp) decreased compared to OVX group (Fig. 7B). This affirms the positive effects of Cur in OP treatment. By comparing OVX + Cur group with OVX + low-dose HCPA NPs group and OVX + high-dose HCPA NPs group, HCPA NPs exerted a stronger anti-bone loss effect than Cur regardless of the dose of HCPA NPs. Meanwhile, high-dosage HCPA NPs had better therapeutic effects than low-dosage group, which seems consistent with the conclusion obtained *in vitro* experiments.

Considering that osteoclasts are key cells that exert bone resorption effects in the progression of OP, we performed H&E staining and TRAP activity staining in tibial tissue sections of mice with different treatment. H&E staining results showed that the OVX group experienced a significant bone loss compared to the sham group. The degree of bone loss was inhibited by drug treatment (Fig. 8A). At the same time, TRAP staining evaluated osteoclast activity. Three fields of view were randomly selected 0.5 mm below the tibial growth plate for TRAP-positive multinucleated cell counting and statistical analysis. As shown in Fig. 8B, we found that osteoclasts decreased significantly after HCPA NPs treatment, indicating that HCPA NPs can exert anti-osteoporotic effects by inhibiting osteoclast activity. Therefore, we can conclude that HCPA NPs synthesized in this work can exert good antiosteoporosis effects *in vivo*, and its therapeutic effect is significantly better than that of free Cur. The therapeutic effect of HCPA NPs on OP depends on the accumulation of Cur and ALN in target tissues and the release the bioactive molecules in target cells. Previous studies have reported that Cur and ALN exert their anti-osteoporosis effects mainly by inhibiting the osteolytic process rather than promoting osteogenesis. Therefore, we believe that the retarding effect of HCPA NPs on bone loss is caused by the combined inhibitory effect of Cur and ALN on osteoclast-mediated bone catabolism. As a novel nanomedicine for clinical applications, its safety *in vivo* should also be evaluated. After treated with HCPA NPs, all mice survived and did not exhibit abnormal behavior. After two months of continuous administration, H&E staining slices from major organs of mice was examined and histopathological evaluation results were shown in Fig. 8C. All treatment groups exhibited a histological morphology similar to the control group, with a clear cell structure and normal nuclei morphology. No cell atrophy, edema, degeneration, necrosis, or other cytopathological changes were found. The above results suggested that administration of HCPA NPs at therapeutic concentrations will not cause a life-threatening problem to laboratory animals, and no obvious toxic side effects were observed after repeatedly administration. In other word, HCPA NPs are a relatively safe and low-toxicity synthetic nanomedicine with good efficacy for OP treatment. Thus, we believe that HCPA NPs are promising for treatment of bone-related diseases owing to the its bone-targeting ability, pH-responsive release behavior, improved bioavailability and low toxicity. Moreover, the strategy developed in this work should also be interest for fabrication of many other drug delivery systems because of its simple operation procedure, mild experimental conditions and good substrate adoptability.

4. Conclusions

The development of highly efficient and biocompatible therapeutic agents for treatment of OP is of great importance and has attracted great research interest. In this work, we developed a simple strategy for construction of a novel pH-responsive bone-targeted DSFDS (named as HCPA NPs) with high drug loading capability. The HCPA NPs is expected to overcome the issues, such as poor water solubility and bioavailability of Cur for in practical using. By taking advantage of the specific reaction activity of HCCP, we conjugated Cur, NH_2-PEG and ALN together using HCCP as the linker. Owing to the introduction of NH_2-PEG, HCPA NPs displays excellent water dispersibility, small particle size (181.9 ± 25.9 nm) and obvious improvement of bioavailability *in vivo*. On the other hand, HCPA NPs exhibit good bone-targeting ability owing to its surface functionalization with ALN. After accumulation at targeted sites and internalization by bone cells, the bioactive compounds Cur will release relied on the hydrolysis of P–O and exert its effects via adjusting the activity of osteoclast and osteoblast. Furthermore, based on the results

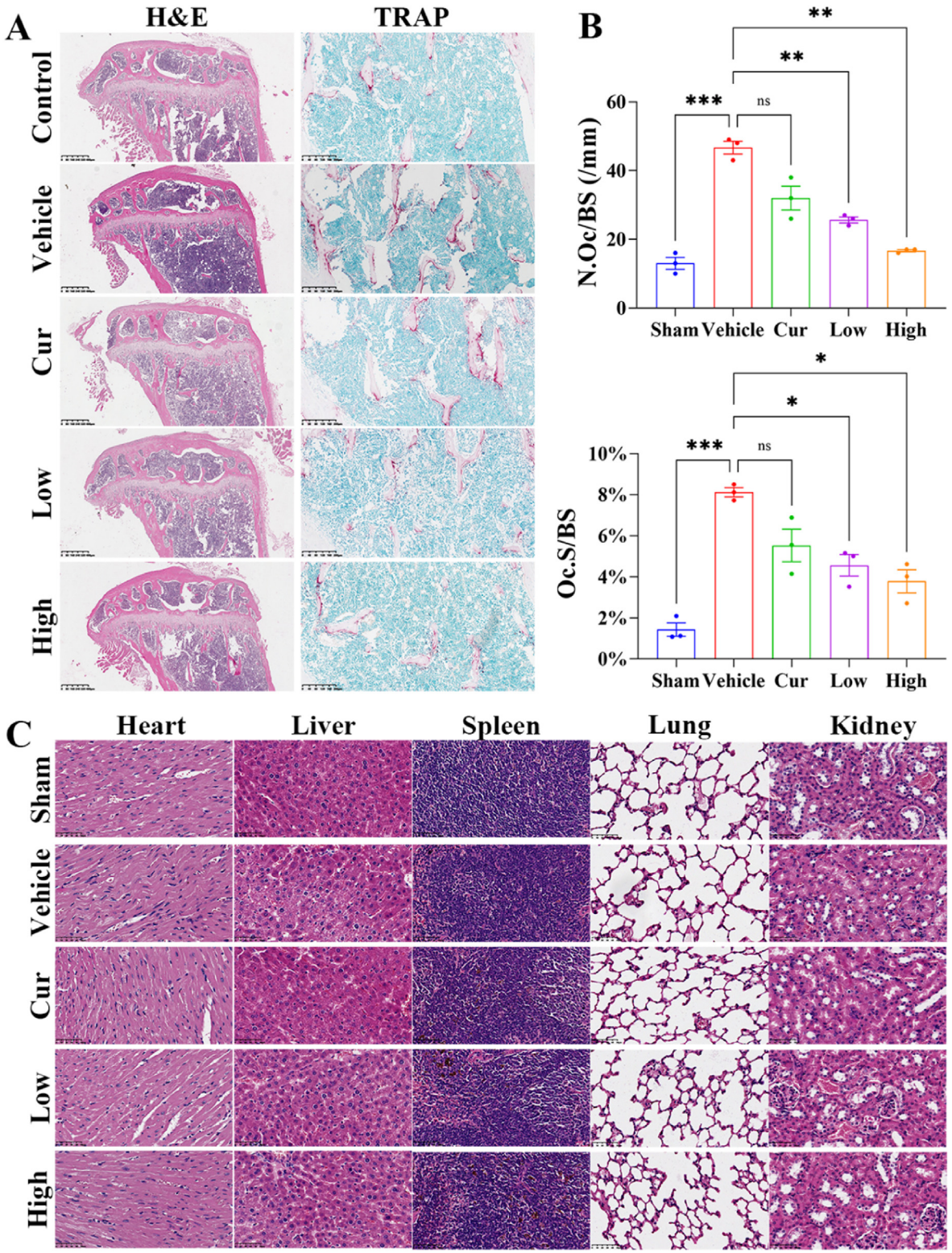

Fig. 8. (A) Histological staining of tibiae from each group of mice eight weeks after surgery was taken to evaluate the volume of trabeculae and osteoclast formation below the tibial growth plate. Scale bars = 400 μm, 200 μm (B) The quantification analysis of the osteoclast surface per bone surface (Oc.S/BS) and the number of osteoclasts normalized to the bone surface (N.Oc/BS). (C) The main organs of each group of mice were stained with H&E 8 weeks after surgery to evaluate organ damage. Scale bar = 50 μm. (All data are expressed as mean ± standard error. *$p < 0.05$, **$p < 0.01$, ***$p < 0.001$ and ****$p < 0.0001$; ns indicates no significant difference).

from *in vitro* and *in vivo* experiments, we demonstrated that HCPA NPs has excellent bone-targeting ability and can effectively reduce bone loss in OVX mice with low toxicity to the major organs. Taken together, we developed a simple but efficient strategy for fabrication of DSFDS with excellent physicochemical properties, high therapeutic effects and low toxicity. This strategy is expected to fabricate many other DSFDS with great potential for treatment of many other diseases.

Credit author statement

Xinmin Yang, Xiaowei Yang: Investigation; Methodology; Writing – original draft. Peng Luo, Yanlong Zhong: Investigation; Methodology. Bin Zhang, Weifeng Zhu, Yen Wei: Project administration; Funding acquisition; Resources; Data curation. Xiaoyong Zhang, Meiying Liu: Conceptualization; Funding acquisition; Supervision; Writing – review & editing. Qi Lai: Conceptualization; Funding acquisition; Supervision.

Declaration of competing interest

The authors declare that they have no known competing financial interests or personal relationships that could have appeared to influence the work reported in this paper.

Data availability

Data will be made available on request.

Acknowledgements

This research was supported by the National Natural Science Foundation of China (Nos. 81860405, 218650165, 21788102, 21967016, 22261035, 22265019) and Natural Science Foundation of Jiangxi Province (Nos. 20181ACB20024, 20171BAB205031).

References

[1] Y. Yu, et al., Cell Metabol. 29 (4) (2019) 966.
[2] L.A. Burt, et al., JAMA 322 (8) (2019) 736.
[3] Y. Zhang, et al., Biomaterials 33 (28) (2012) 6698.
[4] C. Chevalier, et al., Cell Metabol. 32 (4) (2020) 575.
[5] Y.S. Yang, et al., Nat. Commun. 10 (1) (2019) 2958.
[6] C. Liang, et al., Nat. Commun. 9 (1) (2018) 3428.
[7] N.B. Binder, et al., Nat. Med. 15 (4) (2009) 417.
[8] Y.H. Hsu, et al., J. Exp. Med. 208 (9) (2011) 1849.
[9] D.M. Black, C.J. Rosen, N. Engl. J. Med. 374 (3) (2016) 254.
[10] H.G. Bone, et al., Lancet Diabetes Endocrinol. 5 (7) (2017) 513.
[11] H.G. Bone, et al., Lancet Diabetes Endocrinol. 5 (10) (2017) 768.
[12] S.R. Cummings, et al., N. Engl. J. Med. 362 (8) (2010) 686.
[13] P. Li, et al., Nat. Commun. 12 (1) (2021) 4499.
[14] L.J. Ma, et al., J pharmaceutical analysis 12 (4) (2022) 683.
[15] A.K. Singh, M. Vinayak, Neurochem. Res. 40 (3) (2015) 463.
[16] A. Hesari, et al., J. Cell. Biochem. 119 (10) (2018) 7898.
[17] L. Das, M. Vinayak, Int. Immunopharm. 20 (1) (2014) 141.
[18] K.M. Nelson, et al., J. Med. Chem. 60 (5) (2017) 1620.
[19] P. Anand, et al., Mol. Pharm. 4 (6) (2007) 807.
[20] M.A. Bill, et al., Mol. Cancer 9 (2010) 165.
[21] E. Blanco, et al., Nat. Biotechnol. 33 (9) (2015) 941.
[22] Y. Barenholz, J. Contr. Release 160 (2) (2012) 117.
[23] Q.J. He, J.L. Shi, J. Mater. Chem. 21 (16) (2011) 5845.
[24] S. Honary, F. Zahir, Trop. J. Pharmaceut. Res. 12 (2) (2013) 255.
[25] V. Mishra, et al., Pharmaceutics 10 (4) (2018) 21.
[26] S. Sevenson, D.A. Tomalia, Adv. Drug Deliv. Rev. 64 (2012) 102.
[27] N. Li, et al., Angew. Chem.-Int. Edit. 53 (7) (2014) 1756.
[28] Z.H. Zhao, et al., Mater. Today Bio 13 (2022) 15.
[29] F. Wang, et al., Biosafety and Health 4 (2) (2022) 79.
[30] W. Li, et al., Biosafety and Health 4 (2) (2022) 95.
[31] Z. Li, et al., Biosafety and Health 4 (2) (2022) 105.
[32] J. Ding, et al., Biosafety and health 4 (2) (2022) 59.
[33] M. Elsabahy, K.L. Wooley, Chem. Soc. Rev. 42 (12) (2013) 5552.
[34] R. Duncan, Nat. Rev. Cancer 6 (9) (2006) 688.
[35] D. Landesman-Milo, D. Peer, J. Contr. Release 161 (2) (2012) 600.
[36] K.M. Cai, et al., J. Am. Chem. Soc. 137 (10) (2015) 3458.
[37] J.F. Zhang, et al., Nanoscale 7 (32) (2015), 13503.
[38] S.Y. Qin, et al., Biomaterials 112 (2017) 234.
[39] S. Chen, et al., J. Math. Chem. B 7 (5) (2019) 778.
[40] J.G. Li, et al., Mol. Pharm. 17 (2) (2020) 710.
[41] J.G. Li, et al., Colloid Surf. B-Biointerfaces 192 (2020) 7.
[42] X.M. Li, P. Liu, J. Math. Chem. B 10 (15) (2022) 2926.
[43] X.B. Xu, et al., J. Math. Chem. B 6 (47) (2018) 7842.
[44] S.L. Hou, et al., ACS Appl. Mater. Interfaces 10 (31) (2018), 25983.
[45] M. Deng, et al., Adv. Funct. Mater. 21 (14) (2011) 2641.
[46] S. AbuMoussa, et al., J. Orthop. Res. 36 (12) (2018) 3294.
[47] T.K. Ryu, et al., J. Contr. Release 232 (2016) 152.
[48] T. Urbaniak, W. Musiał, Nanomaterials 9 (9) (2019) 1240.
[49] D.G. Jeung, et al., Nanomaterials 9 (9) (2019) 1262.
[50] Q. Yan, W. Sang, Chem. Sci. 7 (3) (2016) 2100.
[51] P. Bélteky, et al., Int. J. Nanomed. 16 (2021) 3021.
[52] L. Tan, et al., Theranostics 7 (10) (2017) 2652.
[53] T. Yang, et al., Drug Deliv. 27 (1) (2020) 575.
[54] C.J. Hu, et al., Sci. Rep. 7 (1) (2017), 13043.
[55] G. Yang, B. Yin, Sci. Rep. 7 (1) (2017) 5982.
[56] S. Rostami, et al., Bioimpacts : BI 12 (4) (2022) 301.
[57] J.L. Nichol, H.R. Allcock, Eur. Polym. J. 62 (2015) 214.
[58] Y.C. Fu, et al., Acta Biomater. 10 (11) (2014) 4583.
[59] E. Wang, et al., Molecules 24 (16) (2019) 2968.
[60] G. Varan, et al., Nanomaterials 8 (2) (2018) 67.
[61] M. Nakamura, et al., Biomed. Res. 42 (1) (2021) 13.
[62] L.B. Solberg, et al., Calcif. Tissue Int. 94 (5) (2014) 510.
[63] J. Yang, et al., Methods Mol. Biol. 2019 (1882) 143. Clifton, N.J.
[64] R.S. Kadzik, et al., Annu. Rev. Cell Dev. Biol. 36 (2020) 35.
[65] H.J. Park, et al., Int. J. Mol. Sci. 18 (3) (2017) 495.
[66] L. Duan, et al., Arthritis Res. Ther. 22 (1) (2020) 279.
[67] D. Xiao, et al., Mol. Med. Rep. 22 (2) (2020) 1536.
[68] D.E. Place, et al., Nat. Commun. 12 (1) (2021) 496.
[69] C. Nottmeier, et al., Int. J. Oral Sci. 12 (1) (2020) 35.
[70] W. Sun, et al., Nat. Commun. 13 (1) (2022) 2899.
[71] J. Guo, et al., Cell Death Dis. 11 (10) (2020) 847.
[72] Y. Kim, et al., Int. J. Mol. Sci. 20 (16) (2019) 4038.